Pyrite Dissolution in the Cretaceous Yogou Formation of the Niger (Chad) Basin: Implications for Basin Evolution under a Rift Tectonic Setting

Kabir Shola Ahmed,* Keyu Liu,* Yuchen Fan, Kouassi Louis Kra, Moussa Harouna, Jianliang Liu, Munezero Ntibahanana, Moussa Z. Salim, Justin Jordan Pidho, Melaine Emmanuel Kouame, Hamma Ada Moussa, and Hafizullah Abba Ahmed

ACCESS | Metrics & More | Article Recommendations | SI Supporting Information

ABSTRACT: This is the first study of pyrite minerals in the entire West and Central African Rift System (WCARS). Several polished organic-rich core samples from the Cretaceous Yogou Formation of the Niger (Chad) Basin located in the WCARS were investigated for their pyrite content using FE-SEM and SEM-EDS imaging techniques. An attempt was made to classify the types and provenance of the pyrites and to highlight the control of rift fractures on the oxidation and dissolution of pyrites in the region. Three major types of pyrites are present in the studied formation, including euhedral pyrite (E*Py*) crystals, pyrite framboids (F*Py*), and sunflower pyrites (S*Py*). A statistical analysis of 307 F*Py* shows that the framboids are diagenetically formed with an average diameter of 6.61 μm. S*Py* is present in a relatively low amount compared to framboids. The pyrites underwent a variety of diagenetic modifications, from mechanical compaction to oxidation, dissolution, and recrystallization. Unoxidized pyrites primarily contain Fe, S, and C, but oxidized pyrites also contain O, Al, and Si. There is a strong correlation between the fractures and the spatial distribution of the physicochemical alteration of the pyrite in the study. Dissolution in relatively deep-buried samples occurs mainly along fracture planes. The fractures provide a pathway for oxidants and other metal elements to reach the pyrites. The pattern of pyrite dissolution reflects the timing of fracture formation and fracture activities as a purveyor or drainage for fluids in the organic-rich samples investigated. The pyrites are associated intimately with organic matter (OM); thus, the relationship between the fracture and the pyrites' transformation is significant in the assessment of organic matter preservation at deep-burial depth.
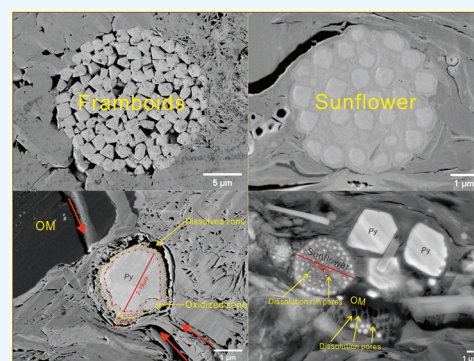
1. INTRODUCTION

Pyrite (*Py*), a naturally occurring iron disulfide (FeS$_2$) mineral, is quite common in marine and terrestrial sediment deposits.[1,2] *Py* can exist in many forms, such as euhedral pyrite (E*Py*) crystals, pyrite framboids (F*Py*), worm shapes, irregular masses, botryoidal-subspherical aggregates, fossil casts, and nodules.[3] *Py* has been extensively studied, from its elemental compositions[4,5] to its origins,[5−7] oxidation reactions,[8,9] morphological evolution,[5,10,11] and redox significance.[12,13]

Two forms of *Py*, syngenetic and diagenetic, have been defined based on the interplay of the environment with reactions of sulfates, organic matter (OM), and reactive iron.[14] Syngenetic *Py* is formed in the near-bottom water column and sediment−water interface that is saturated with H$_2$S[14,15] and preserved in the underlying sediment,[12] while diagenetic *Py* is usually formed from OM decomposition in an anaerobic sedimentary environment that has sufficient H$_2$S and water. *Py* in the marine environment is formed largely by microbial sulfate reduction in the subsea environment.[16,17] In a petroliferous basin, *Py* has an intimate relationship with OM, as both *Py* and OM degradation

in sediments is through microbial reduction of seawater sulfate,[17,18] and the sulfide product is preserved either as *Py* or inorganic sulfur (S) compounds.[18]

Py is a hard-to-dissolve mineral stable in an anoxic environment across a range of pH and Eh values.[16] It has a very low solubility.[19] However, through chemical oxidation and reduction reactions, it can be oxidized and dissolved. The degree of dissolution observed for *Py* is controlled by a variety of factors, including its exposure to oxygen and water,[20−22] oxygen concentration,[23] presence of sulfate-reducing bacteria,[24,25] bacterial action and sediment Ph,[24,25] basin temperature,[26,27] concentration of Fe(II),[23,24] continuous supply of H$_2$S$_2$,[28] and
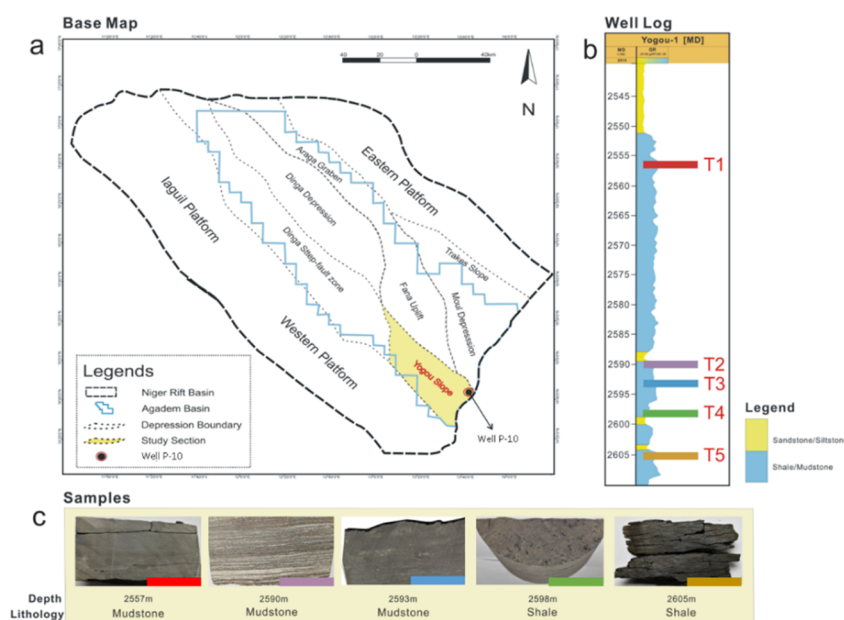
Figure 1. (a) Base map of the Agadem Basin showing the location of the studied well (P-10) in the yellow grid. (b) γ-ray log curve showing the lithology and corresponding depth of rock samples examined. (c) Depth and lithology labels of the core samples analyzed.

degree of stress which affects the Fe and S_2 film and *Py* double layers.[29]

In an experiment conducted to test the bacterial leaching efficiency on *Py*, a pH value range of 1.1−2 gave the best efficiency,[24] while dissolution efficiency dropped when Fe(III) attained a concentration of 35 g L^{-1} and Fe(II) attained that of 27 g L^{-1}.[24] The continuous increase in Fe concentration reverses the leaching process by clogging the surface of the *Py*.[28] Several factors affect the oxidation and dissolution of *Py*; factors such as redox conditions,[12,27] pH,[20,21] organic matter,[30,31] particle size,[28] and oxidizing bacteria,[30] among others, have been advanced by sulfide petrologists. In this study, we concentrated on the effect of rock fractures on *Py* alteration within a sedimentary basin to emphasize the special petrographic relevance of tectonic-induced rock fractures on *Py* oxidation and dissolution in a petroliferous basin.

## 2. GEOLOGICAL BACKGROUND OF THE NIGER RIFT BASIN

The rift basin of Niger belongs to the series of Africa Cretaceous basins unified by extensional tectonics leading to the breaking away of the South American plate from the African plate.[32] Extensional tectonics in the Paleozoic and Cretaceous (550−75 Ma) led to the formation and expansion of the Niger (Chad) Basin to form an intracontinental deposit consisting of gray lacustrine mudstone interbedded with sandstone deposits.[33] The south section has the deepest sediment deposits (over 13 km) with both marine and terrestrial sediments.[34] The basin has experienced significant tectonic and thermal subsidence in the Cretaceous, followed by a tectonic uplift and erosion in the Paleogene, causing significant destruction to its petroleum potential in the northern section.[34] Generally, the basin has an average surface temperature of 23 °C[35] with sediments enriched with terrigenous organic matters, planktons, and freshwater algae from a fresh to brackish oxic environment restricted from seawater exchange with the Tethys and the Atlantic Ocean surrounding it.[36]

3. METHODS

3.1. Data Preparation. The mudstone and shale samples studied were organic-rich core samples collected from five different depth intervals (2557, 2590, 2593, 2598, and 2605 m) along Well P-10 in the Niger (Chad) Basin made available by the Niger Ministry of Petroleum (Figure 1). The different depths are respectively labeled T1− T5 and referred to accordingly in the proceeding reports. The core samples represent the transitional marine environment rocks in the southern Niger (Chad) Basin with macro- to micro-scale fractures.[33] The samples cover 48 m of core length and comprise four rock facies, including clay-rich sandstone, laminated muddy sandstone, siliceous mudstone, and shale.[33] The samples analyzed (Figure 1c) were from the mudstone and shale sediment sections. The samples were prepared as polished sections using a fully automated argon ion milling system (PEC II Model 685) to obtain high-quality polished samples. The samples were then placed into an ion sputter coater (ISC-150 Pro) device, carbon-coated, and afterward were observed using a field emission scanning electron microscope (FE-SEM) and scanning electron microscope energy dispersive X-ray spectroscopy (SEM-EDS). The coating enhances the image quality and resolution by increasing the signal-to-noise ratio during SEM imaging, which results in a better quality image.

3.2. Scanning Electron Microscopy (SEM) Analysis. SEM is a high-resolution petrographic microscope highly suitable for mineral surface and shape analysis. Combined with the EDS technique, it allows both qualitative and quantitative *in situ* chemical analyses to be conducted. Using a high-resolution version of FE-SEM (Zeiss Crossbeam 550) by Carl Zeiss Microscopy, the T1−T5 samples (Figure 1c) were observed for their pyrite (*Py*) contents, fractures, *Py* alteration, and relationship to ambient fractures.

3.3. Energy Dispersive X-ray Spectroscopy (EDS) Analyses. A point analysis of oxidized and unoxidized zones on pyrite (*Py*) samples was carried out to examine the chemical compositions and elemental distinction between the two zones. In this method, visual inspection of a sample is accomplished by
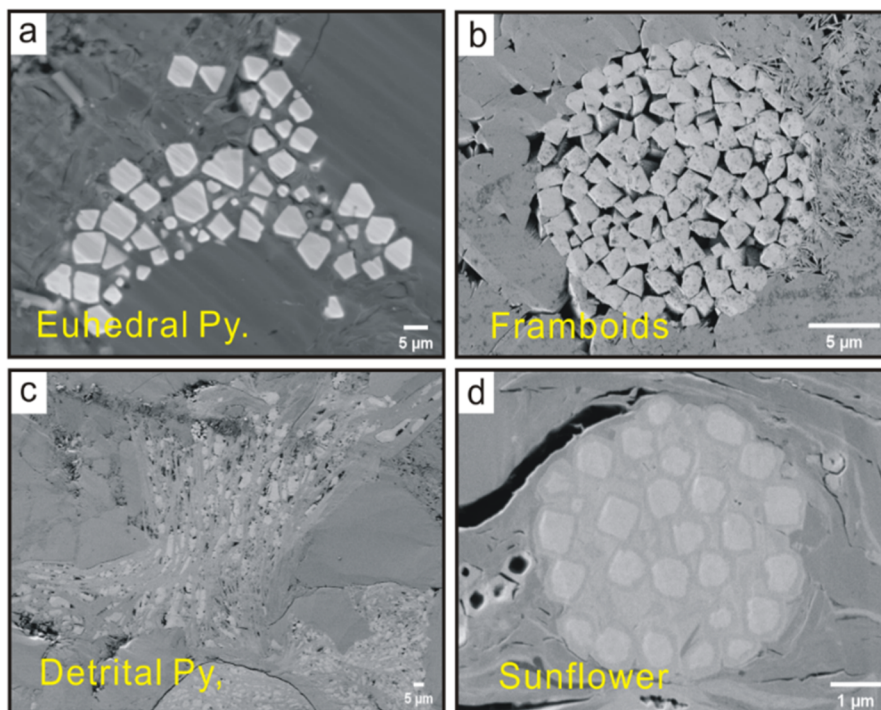
Figure 2. Scanning electron microscopy images of pyrite (*Py*) types (scale bar: 1−5 μm): (a) monocrystal or euhedral pyrite (E*Py*s) formed along fracture planes; (b) pyrite framboids (F*Py*) in host rock; (c) cataclastic aggregates of detrital pyrites (D*Py*s) occurring as fracture-filling minerals; (d) sunflower pyrite (S*Py*)—F*Py* with an outer crystal.

focusing the electron beam on a particular area of the image of the sample obtained by a scanning electron microscope. This causes an atom to be displaced, creating a positive charge in the atom's inner shell, which is then replaced by another electron from an outer shell. The EDS equipment automatically performs the analysis up to the resolution limit of ≤2 μm and saves both the location and the associated EDX spectra, revealing the compositional ratios (atomic ratios) of every element discovered in the point scan. However, electron shielding in samples containing multielectron ion elements with large changes in the Z number, low concentrations of an element, and other factors could alter the results of the EDS examination.

3.4. Statistical Analysis of Pyrite Framboids Using ImageJ and Origin Software. The ImageJ and Origin programs were employed to process and analyze the pyrite framboids (F*Py*) images obtained from the SEM/EDS analyses. They were used for redox condition prediction based on the importance of F*Py*s for paleo-redox condition prediction and its relatively higher susceptibility to chemical diagenesis. Three hundred and seven F*Py*s were labeled with their diameter measured using the ImageJ software. The data collected were saved (CSV file) and then analyzed statistically using the Origin software. The average diameter of the 307 F*Py*s was then plotted on a histogram normalized by a Gaussian distribution function plot.

Where 30 to more than 100 F*Py*s diameter measurements were used for paleo-redox condition prediction, errors due to irregular crystal morphologies, distorted minerals, and human errors were significantly reduced and the data set and subsequent analysis and interpretation were enhanced.[37] Therefore, the number of F*Py*s used for this study is within a reasonable limit and the interpretation adopted a log-normal distribution,[37,38] which is a good fit for SEM image sets.[37]

4. RESULTS

**4.1. Pyrite Varieties Discovered in the Samples Analyzed.** Variable-size E*Py*s and F*Py*s were found in T1, T2, T3, T4, and T5, and detrital pyrites (D*Py*s) in T2, T3, and T4. E*Py* is found to be predominant in T5. The *Py*s are formed along fracture planes as clusters of individual forms such as E*Py*s (Figures 2a), F*Py* (Figure 2b), D*Py*s (Figure 2c), and S*Py* (Figure 2d) and sometimes as aggregates of *Py*s coexisting with OM (Figure 3). In T2 and T4 mudstone samples, D*Py*s predominate and exist primarily as cement (Figure 2c). S*Py*s and aggregations of F*Py*s known as "polyframboids" were observed in the shale samples T4 and T5 (Figure 3). F*Py* is formed at a high saturation of iron monosulfide,[6] exhibiting semispherical and spherical shapes within the host rock and OM (Figures 2b and 3). By transforming into a core—shell structure *Py*, E*Py* and
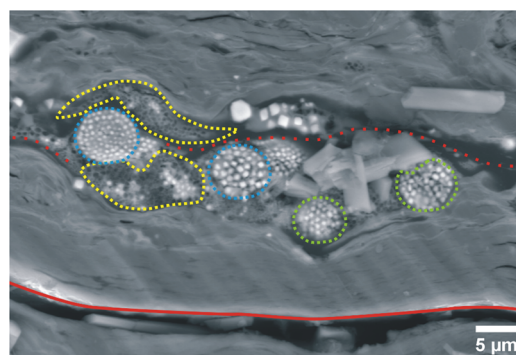

Figure 3. Polyframboids showing degraded pyrite framboids (F*Py*s) (yellow grid) with dissolutional cores and orderly arranged pyrite framboids (F*Py*s) (blue grid) and disorderly arranged pyrite framboids (F*Py*s) (green grid) within an organic matter (OM) filled fracture (red dashed line) and open fracture (red line).
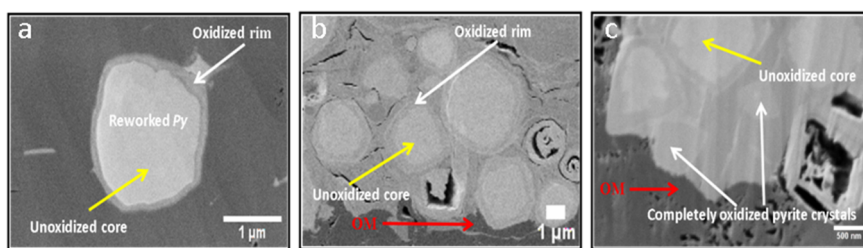
Figure 4. SEM images of (a) rough edge or reworked pyrite (*Py*) with an unoxidized core and oxidized rim, (b) regular shape or euhedral pyrite (E*Py*) with an unoxidized core and oxidized rim, (c) nanomicron crystals of sunflower pyrite (S*Py*) with completely oxidized *Py* crystals and dissolved cores.
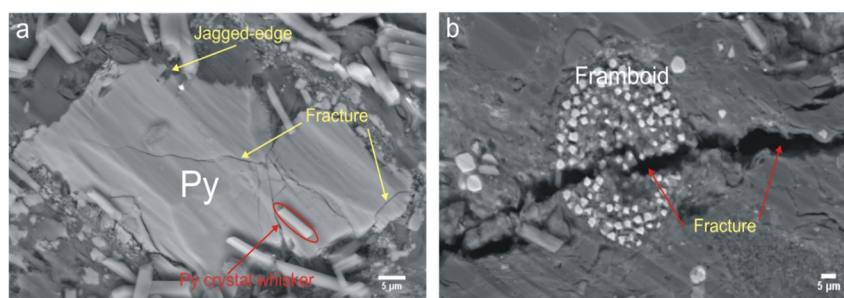
Figure 5. Fractures dissecting (a) a jagged-edge or reworked eudrehal pyrite crystal (E*Py*) surrounded by *Py* whiskers (W*Py*s), randomly arranged thick bar *Py* crystals, and (b) degraded pyrite framboids (F*Py*).
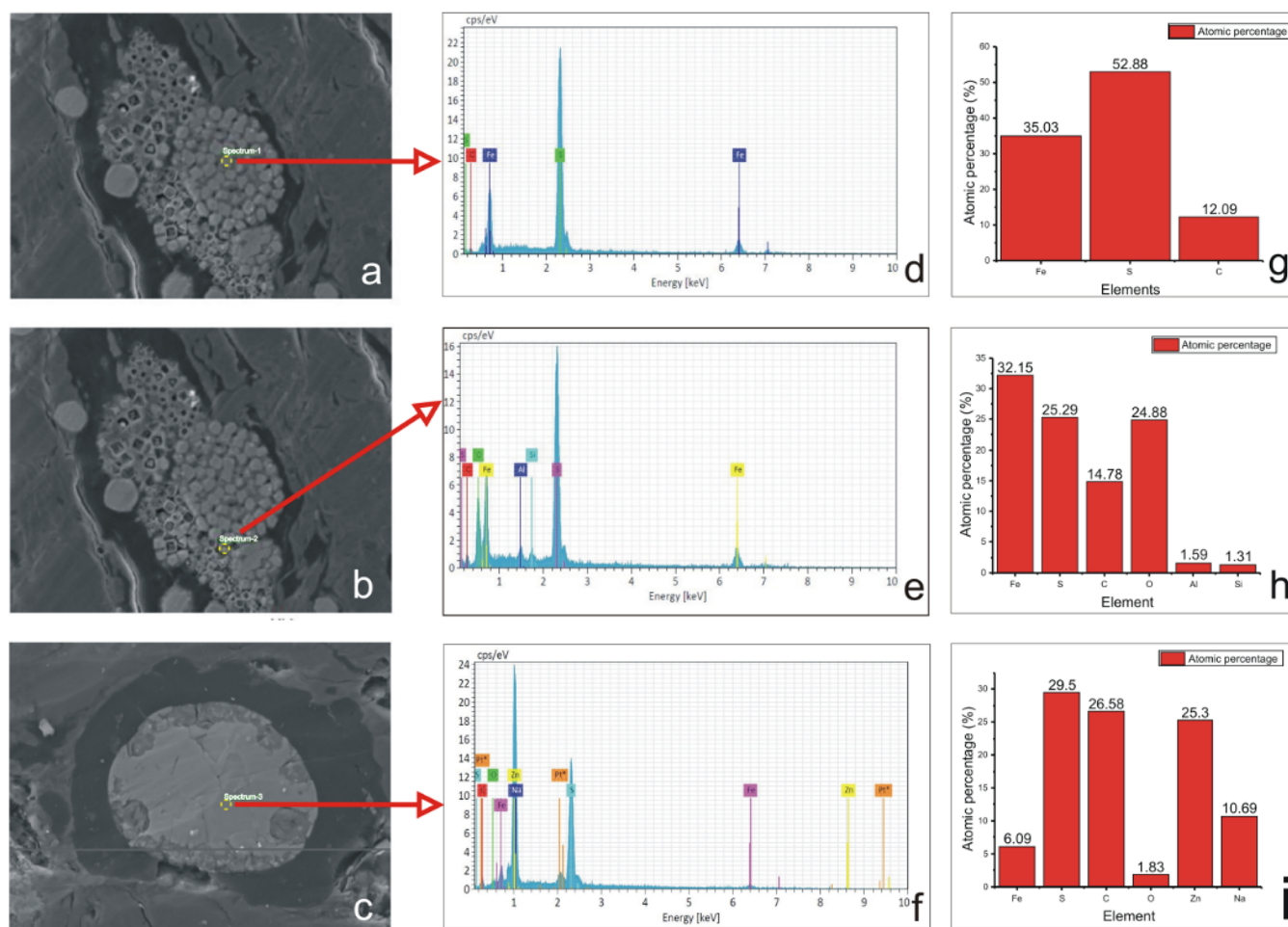
Figure 6. Energy spectrum component analyses for (a,b) pyrite framboids (F*Py*s) and (c) cuhedral pyrite (E*Py*) showing the location of the mineral inclusion point scanned for the atomic number and chemical composition of the inclusion. (d−f) EDX spectra showing the compositional ratios (atomic ratios) of all the elements detected in the point scans. (g−i) histogram plots of atomic percentage (at. %) of elements in the analyzed samples.
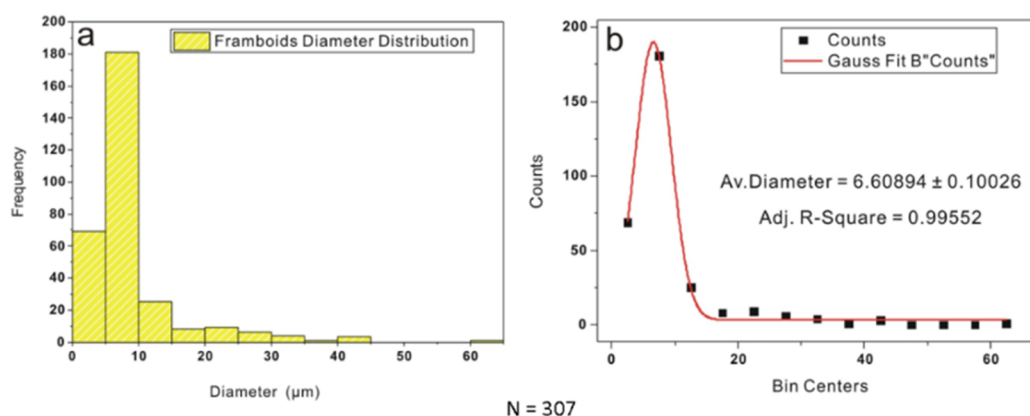
Figure 7. Relative frequency and diameter distribution of 341 pyrite framboids (F*Py*s) analyzed. (b) Gaussian distribution function showing the average diameter (average diameter) of F*Py*s. *N* is the number of samples.

Table 1. Petrographic Features and Distribution of Pyrite Types from Core Samples of the Well P10 with a Focus on Its Transitional Formation Zone

	size		diagenetic sequence					
pyrite type	range (μm)	av diameter (μm)	compaction	oxidation	dissolution	surface morphology	environment	remark
monocrystal (E*Py*)	not measd	not measd	low	low to high	low to high	jagged-edge, rim pore, core pore, surface fracture	continental/marine	present at all depths
detrital (D*Py*)	not measd	not measd	rare	rare	rare	jagged-edge, surface fracture	continental/marine	widespread at depth 2590 m
framboid (F*Py*)	0.061−63.229	6.61	moderate	low to moderate	moderate	rim pore, core pore, surface fracture	continental/marine	present at all depths, predominant at depth 2605 m
sunflower (S*Py*)	2.092−12.927	7.12	high	high	high	rim pore, core pore, surface fracture	continental/marine	found only at depth *2605 m*

F*Py* can develop into S*Py* (Figure 4a−c).[39,40] Figure 2a shows single crystals of (Fe(II)) polysulfide (E*Py*) under normal saturation, while Figure 2b shows a single crystal of (Fe(II)) polysulfide (F*Py*) under rapid nucleation[7] of supersaturated iron monosulfide.[41,42] Both E*Py* and F*Py* crystals can coexist (Figure 3).

F*Py* falls to normal saturation when supersaturated FeS₂ develops (Figure 3). The drop could be attributed to a decrease in sulfate-reduction-bacterial (SRB) activity or a depletion of the Fe source.[41] As a result, when completely grown (blue bar, Figure 3), some F*Py* (ordered-F*Py*) may appear as spherical clusters of E*Py*[43] and semispherical for partially formed or decaying F*Py* (yellow bar; Figure 3). Polyframboids are a collection of F*Py*s that are typically formed in OM, where thermal fluid and sulfate-reduction-bacterial (SRB) processes are engaged in the development of E*Py* from F*Py* and cement *Py*.[5] In zones of significant tectonic activity, D*Py* (Figure 2c) and pyrite whiskers (W*Py*s) (Figure 5) are widespread.

4.2. Organic Matter in the Samples Analyzed. Bitumen is the most abundant organic matter type in all of the tested samples with a few structured and amorphous kerogens.[33] They are randomly spread across the surface of the shale and mudrock samples systematically in association with *Py* inclusion (Figure 3). A part of the bitumen forms a regular pattern along fracture planes on the host rock.

4.3. Rock Fractures in the Samples Analyzed. Fractures of diverse sizes and forms are extensively distributed across the samples. Many of the fractures found were open (Figure 3), and a few ran along the bitumen and host rock boundary, while others cut through bitumen and *Py*. The sample T5 appeared to

be the most fragmented, with mineral infillings ranging from E*Py* to F*Py*, W*Py*, and OM. Premineralization fractures and postmineralization fractures are the two types of fractures that have been observed. The first group are filled with OM, *Py*, kaolinite, and other mineral inclusions (Figures 2a,c and 3), whereas the second category cut through the OM and mineral inclusions—E*Py* and F*Py* (Figure 5a,b), showing that they were formed after the *Py*s.

4.4. SEM/EDS Elemental Composition Analysis Results. A point analysis was performed on selected *Py* minerals (Figure 6a−c) to obtain their elemental compositions in order to improve our understanding of the chemical nature of the *Py* in the study area. The minerals were excited with 10.0 keV electron beam energy from a scanning electron microscope (SEM) to obtain their elemental compositions. The resulting X-ray energy spectra (Figure 6d−f) as well as a table of constituent element weight percentage (wt. %) and atomic percentage (at. %) were examined. In a histogram, the at. % for each element is shown (Figure 6g−i). The effect of electron shielding in multielectron ion elements with considerable variances in the Z number, element in an aqueous solution, and overlap of a given spectral line can cause uncertainty in the results of EDS analyses. Except for $Z = 8.630$, which falls into the energy range of 6−7 keV, all of the samples detected have low emission energy in the range of 1−3 keV. There is no overlap between the spectral lines, providing for the optimum outcomes.

4.5. Pyrite Framboid Size Distribution Results. F*Py*s were selectively analyzed as an indicator of paleo-redox conditions of sediments[12,44] and paleowater.[45] Following a statistical analysis of the sizes and distributions of 307 F*Py*s from
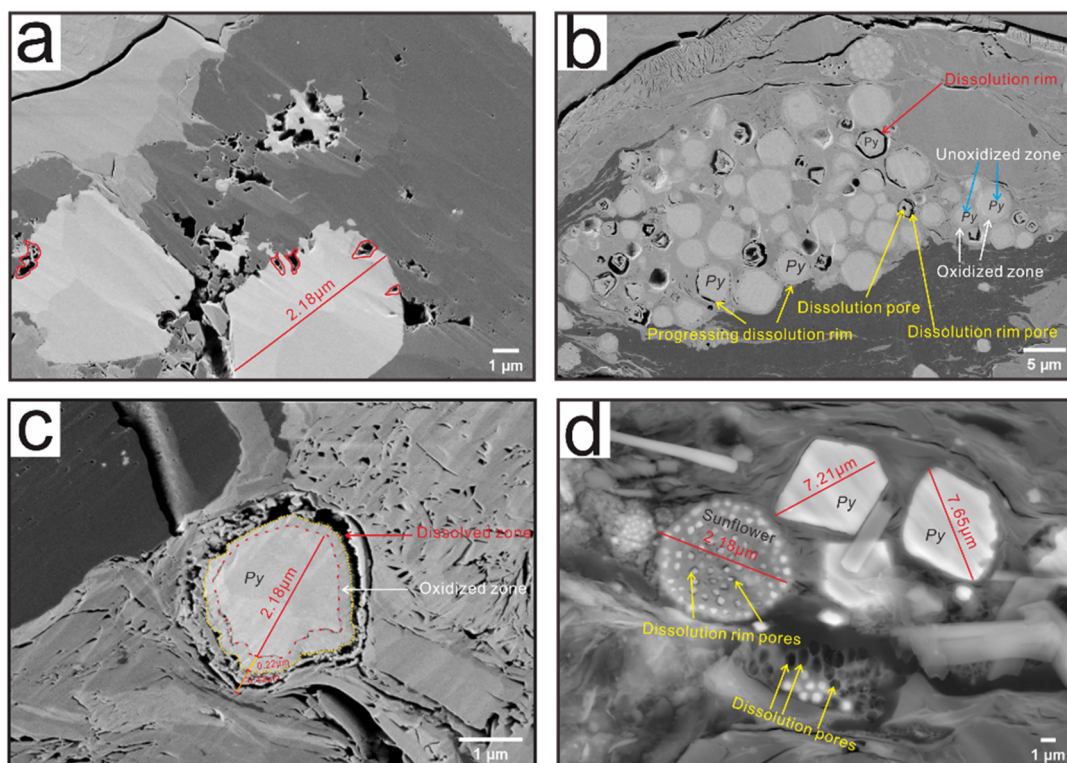
Figure 8. SEM images showing the different forms of chemical diagenesis observed in the well P-10 core samples. (a) Dissolution of the mineral framework on a typical pyrite (*Py*) crystal within organic materials (OM). (b) Oxidized euhedral pyrite (E*Py*s) crystals undergoing core and rim dissolution. (c) Euhedral pyrite (E*Py*) along the fracture plane showing three concentric zones; dissolved outer zone, oxidized core−shell, and unoxidized core. (d) In open fractures, both sunflower pyrite (S*Py*) and pyrite framboid (F*Py*) exhibit different degrees of mineral dissolution, with considerable rim dissolution in the case of S*Py*s and complete mineral dissolution in the case of F*Py*s.

the examined samples, the following findings are presented. According to a histogram plot of the F*Py*s' diameters, the F*Py*s have a diameter ranging from 2.84 to 62.51 μm (Figure 7a). The standard deviation is 5.69 μm, and the average diameter is 6.61 μm (Figure 7b and Table 1). T5 has the smallest F*Py*, while T1 has the largest diameter. F*Py*s smaller than 1 μm are considered to be very small, those between 1 and 3 μm are considered small, those between 3 and 10 μm are considered medium-sized, and those larger than 100 μm are considered very large.[46]

Except for T1, F*Py*s larger than 25 μm (Figure 7a) were uncommon in the other sections investigated. F*Py*s are typically 5−6 μm in length,[47] and their size range overlaps those of syngenetic and diagenetic F*Py*s, which are 2.9−10.9 and 3.1−20.9 μm, respectively.[37] The average particle sizes of F*Py*s in a confined basin or euxinic system are mostly 6 μm[47,48] and remain constant irrespective of diagenetic processes,[12] making them a useful tool for distinguishing between oxic and anoxic water conditions.[12]

5. DISCUSSION AND INTERPRETATION

Py oxidation and dissolution are distinct processes; however, they are connected by a need for ambient oxygen. When oxidizing *Py* reacts with a high concentration of dissolved oxygen, the rate of dissolution will be favorably increased.[23] Figures 4a−c and 8b show samples of the two most prevalent *Py* forms, E*Py* and F*Py*,[12] that were under investigation in this study. Many of the samples had a concentric oxidation of *Py* minerals, while only a few had dissolution of *Py*-overgrowth or the *Py* crystal core, particularly in the deeply buried *Py*s (T4 and T5). According to Courtin-Nomade et al.[49] and Gu et al.,[50]

monocrystal *Py* oxidation produces *Py* with a core−shell structure or the appearance of two layers, with an unoxidized inner core in the center.[50,51] As seen in this study, dissolution in both E*Py* and F*Py* results in a wide variety of surface morphologies on the E*Py*s and the F*Py*s. Dissolution pores (Figure 8a,b,d), dissolution rim pores (Figure 8b−d), and jagged-edged monocrystals (Figure 8a) are the products of this process. In comparison to S*Py*, which displays a comparatively higher degree of dissolution in its core than in its shell, the other two primary *Py* types, E*Py* and F*Py*, exhibit relatively less dissolution (Figure 4c). F*Py* is more prone to dissolution than is E*Py* (Figure 9). However, the dissolved F*Py* may recrystallize as new E*Py*, a more stable form of *Py* as shown in Figure 8d, where new E*Py*s have sizes of 7.21 and 7.65 μm. The statistical analysis result of the 307 F*Py*s analyzed in this study (Table 2) shows that 89% of the *Py*s are between 2.5 and 12.5 μm. The Gaussian distribution function yielded an average F*Py* diameter of 6.61 μm, with a standard deviation of 5.69. The findings indicate that the size ranges of syngenetic F*Py* (2.9−10.9 μm) and diagenetic F*Py* (3.1−20.9 μm) overlap.

Out of the 307 samples analyzed, 259 samples or 84% overlapped. While 13.68% of them have diameters that are above the high cutoff size for syngenetic F*Py* (10.9 μm), only 1.95% of them are less than the low cutoff size for diagenetic F*Py* (3.1 μm). Therefore, the diagenetic F*Py* appears to prevail.

The study's average F*Py* diameter (6.61 μm) and the world's average diameter for diagenetic F*Py* (6.7 μm) reported by Rickard[37] differ by 0.09 μm. The agreement between these two averages verifies the precision of the measurements and the methods used for analysis in this study. The relative abundance
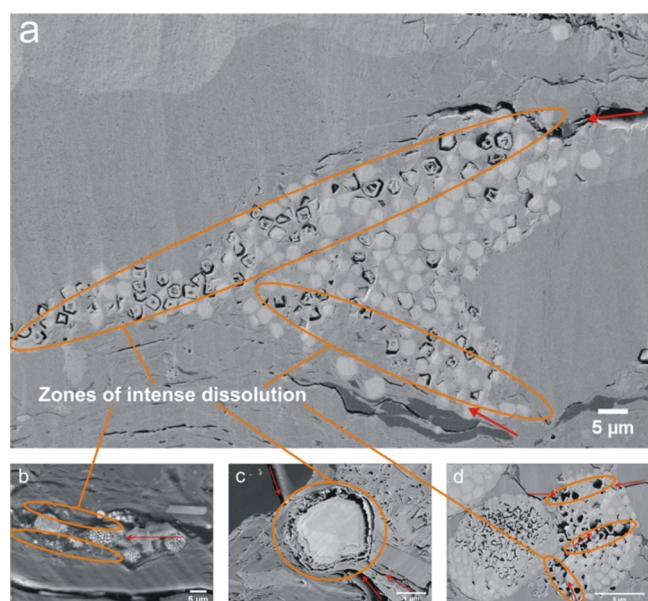
Figure 9. (a) Preferential intensive dissolution of monocrystal pyrites along a healed-fracture path. (b) Polyframboids showing a high degree of mineral dissolution on framboids formed within a fracture. (c) Fracture-induced rim dissolution of a monocrystal formed along fracture paths. (d) Sunflower pyrites (SPys) showing complete mineral dissolution around the fracture network.

Table 2. Statistics of Pyrite Framboids in the Cretaceous Yogou Formation Showing Normalized Diameter Distributions
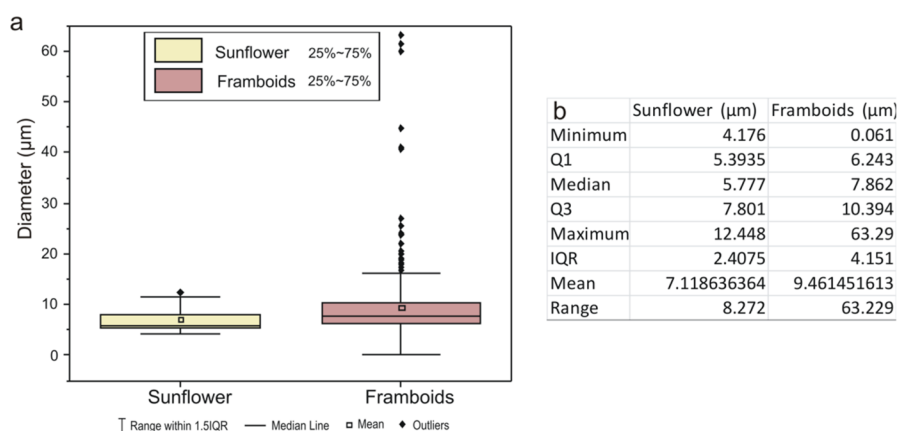
pyrite diameter interval	frequency	diameter (%)
2.5	38	11.14
7.5	204	59.82
12.5	71	20.82
17.5	11	3.22
22.5	9	2.64
27.5	2	0.57
32.5	0	0
37.5	0	0
42.5	3	0.88
47.5	0	0
52.5	0	0
57.5	1	0.29
62.5	2	0.59

of the diagenetic F*Py* indicates that the paleoenvironment was rich in organic matter and had sufficient oxygen circulation, since the formation of diagenetic F*Py* depends on the availability of these two elements under rapid sedimentation.[52]

Variable levels of postformation oxidization have occurred in all of the reported F*Py*s and 70% of the observed E*Py*s. Some *Py* had undergone complete oxidation, while others had incomplete oxidation and showed either a monocrystal with a core−shell structure (Figure 4b,c) or S*Py* (Figure 9d); the F*Py*s may be able to anticipate the abundance of organic matter because they flourish in sediment with high levels of organic matter.[53] In comparison to high-energy-environment sediments (sandstones), low-energy-environment sediments such as claystones, siltstones, and carbonates typically have higher levels of organic matter and more iron minerals for converting sulfates to hydrogen sulfides.[54] Similarly, the presence of organic matter reduces the rate of diagenetic degradation of *Py*.[32]

F*Py* and recrystallized F*Py* with a core and outer crystal (S*Py*) were cross-plotted to ascertain their relationships with size (Figure 10), since S*Py* is a direct product of F*Py*'s overgrowth or recrystallization.[41] Twenty-two S*Py*s were sampled from T5, measured, labeled, and then analyzed for their size distribution. Crystal sizes between 6 and 7 μm were predominant. The largest S*Py* has a diameter significantly smaller than the large-diameter F*Py* in the study (Figures 10a,b). The result suggests that in a given range of F*Py*s having random crystal diameters recrystallization affects the small-sized crystals more than the large-sized crystals, except for where large-sized *Py* crystals exist where recrystallization is enhanced: i.e., close to or along the fracture plane.

The reported impact of fracture on the dissolution of *Py* helped establish the connection between *Py*s and tectonic activity. Every sample has some level of fracturing. Zones of significant tectonic activity frequently include the D*Py*s and W*Py*s observed in this study (Figure 2c and 5a). Many open fractures were observed on the host rock and *Py* crystals (Figures 5a,b). Old fractures were filled with clay minerals and *Py*s (Figure 2a,c and 3). *Py* can weaken rock strength and discharge heavy metals into the environment. The mineral dissolution around the fractures is a noteworthy finding in this investigation. However, a steady decomposition of the *Py* and its associated organic matter under an anoxic condition such as for the investigated samples is linked to the presence and the activities of sulfate reducing bacteria (SRB).[16] However, the open fracture

b	Sunflower (µm)	Framboids (µm)
Minimum	4.176	0.061
Q1	5.3935	6.243
Median	5.777	7.862
Q3	7.801	10.394
Maximum	12.448	63.29
IQR	2.4075	4.151
Mean	7.118636364	9.461451613
Range	8.272	63.229

Figure 10. (a) Box plot and (b) table showing the minimum, median, and maximum sizes of sunflowers (S*Py*s) and framboids (F*Py*s) in the well P10.

pathways were discovered to have a rather high level of pyrite mineral degradation (Figure 9).

Due to the fact that *Py* located far from the fracture zones does not undergo major physicochemical changes, the dissolutions described here are confined and unusual. As a result, the preferential dissolution of *Py*s along the healed fracture paths (Figure 9a), OM-filled fracture (Figure 9b), and open fracture (Figure 9c,d) is proof that the presence of a fracture actually causes and sustains *Py* mineral dissolution in the study area by creating pathways for degradant fluids to reach the *Py* crystal.[29,51] However, more investigation into the effects of fracture/microcracks on *Py* at the grain level is advised, utilizing a more sophisticated microstructural analysis approach, such as electron backscatter diffraction (EBSD).

6. CONCLUSIONS

The Cretaceous Yogoou Formation has five forms of pyrites: euhedral crystals, framboids, sunflower, detrital, and whiskers. The presence of detrital pyrite and pyrite whiskers is a reliable sign of high tectonic activity, implying that the fractures seen are tectonically produced.

According to the diameter size distribution of framboids, the majority of pyrite types in the study are diagenetic pyrites generated in organic-rich sediments.

The pyrite redox state and the fractures in the samples have a strong relationship. Even while coexisting organic debris within the fracture channels may attenuate the effect, the fracture boosts oxygenation of the deeply buried Cretaceous Yogou Formation pyrites and systematically increases pyrite dissolution.

The observed pyrite recrystallization and dissolution are valuable tools in determining paleotectonic history.

■ ASSOCIATED CONTENT

Data Availability Statement

All data generated or analyzed during this study are included in this published article.

Ⓢ Supporting Information

The Supporting Information is available free of charge at https://pubs.acs.org/doi/10.1021/acsomega.2c03027.

The measured diameters of selected framboid pyrite and sunflower pyrite minerals and the measured dimensions for the 307 F*Py*s and 22 S*Py*s used in the study's statistical analysis (PDF)

■ AUTHOR INFORMATION

Corresponding Authors

Kabir Shola Ahmed − *School of Geosciences, China University of Petroleum (East China), Qingdao 266580, People's Republic of China;* ⓞ orcid.org/0000-0002-6235-1776; Email: sholli242@yahoo.com

Keyu Liu − *School of Geosciences, China University of Petroleum (East China), Qingdao 266580, People's Republic of China;* ⓞ orcid.org/0000-0002-8741-9802; Email: liukeyu@upc.edu.cn

Authors

Yuchen Fan − *School of Geosciences, China University of Petroleum (East China), Qingdao 266580, People's Republic of China*

Kouassi Louis Kra − *School of Geosciences, China University of Petroleum (East China), Qingdao 266580, People's Republic of China*

Moussa Harouna − *Université Abdou Moumouni, Faculté des Sciences et Techniques, Département de Géologie, BP 10662 Niamey, Niger*

Jianliang Liu − *School of Geosciences, China University of Petroleum (East China), Qingdao 266580, People's Republic of China*

Munezero Ntibahanana − *School of Geosciences, China University of Petroleum (East China), Qingdao 266580, People's Republic of China;* ⓞ orcid.org/0000-0002-2082-0853

Moussa Z. Salim − *Shandong Ginzre New Material Development Co. Ltd., Jinan 271100, People's Republic of China*

Justin Jordan Pidho − *School of Petroleum Engineering, China University of Petroleum (East China), Qingdao 266580, People's Republic of China*

Melaine Emmanuel Kouame − *State Key Laboratory of Biogeology and Environmental Geology, School of Environmental Studies, China University of Geosciences, Wuhan 430074, People's Republic of China*

Hamma Ada Moussa − *Université Abdou Moumouni, Faculté des Sciences et Techniques, Département de Géologie, BP 10662 Niamey, Niger*

Hafizullah Abba Ahmed − *Department of Geology, Modibbo Adama University of Technology, 2076 Yola, Nigeria*

Complete contact information is available at:
https://pubs.acs.org/10.1021/acsomega.2c03027

Notes

The authors declare no competing financial interest.

■ ACKNOWLEDGMENTS

■ REFERENCES

(1) Love, L. G.; Amstutz, G. C. Review of microscopic pyrite from the Devonian Chattanooga Shale and Rammelsberg Banderz. *Fortschr. Min.* **1966**, *43*, 273−309.

(2) Wilkin, R. T.; Barnes, H. L. Formation processes of framboidal pyrite. *Geochim. et Cosmochim. A* **1997**, *61* (2), 323−339.

(3) Siesser, W. G. Petrography and geochemistry of pyrite and marcasite in DSDP Leg 40 sediments. *Initial Reports of the Deep-Sea Drilling Project* 1978, pp. 767−775.

(4) Sykora, S.; Cooke, D. R.; Meffre, S.; Stephanov, A. S.; Gardner, K.; Scott, R.; Salley, D.; Harris, A. C. Evolution of Pyrite Trace Element Compositions from Porphyry-Style and Epithermal Conditions at the Lihir Gold Deposit: Implications for Ore Genesis and Mineral Processing. *Econ. Geol.* **2018**, *113* (1), 193−208.

(5) Yue, L.; Jiao, Y.; Wu, L.; Rong, H.; Fayek, M.; Xie, H. Evolution and origins of pyrite in sandstone-type uranium deposits, northern Ordos Basin, north-central China, based on micromorphological and compositional analysis. *O. Geol.Rev.* **2020**, *118*, 2020.

(6) Wilkin, R. T.; Barnes, H. L. Formation processes of framboidal pyrite. *Geochim. et Cosmochim. A* **1997**, *61* (2), 323−339.

(7) Butler, I. B.; Rickard, D. Framboidal pyrite formation via the oxidation of iron (II) monosulfide by hydrogen sulphide. *Geochim. et Cosmochim. A* **2000**, *64* (15), 2665−2672.

(8) Andersen, M. S.; Larsen, F.; Postma, D. Pyrite Oxidation in Unsaturated Aquifer Sediments. Reaction Stoichiometry and Rate of Oxidation. *Env. Sci. & Technol.* **2001**, *35* (20), 4074−4079.

(9) Du, R.; Xian, H.; Wu, X.; Zhu, J.; Wei, J.; Xian, J.; Tan, W.; He, H. Morphology dominated rapid oxidation of framboidal pyrite. *Geochem,Persp. Lett.* **2021**, *6*, 1.

(10) Liu, Z.; Chen, D.; Zhang, J.; Lü, X.; Wang, Z.; Liao, W.; Shi, X.; Tang, J.; Xie, G. Pyrite Morphology as an Indicator of Paleoredox Conditions and Shale Gas Content of the Longmaxi and Wufeng Shales in the Middle Yangtze Area, South China. *Mins* **2019**, *9* (7), 428.

(11) Meng, L.; Huang, F.; Wang, X.; Gao, W.; Zhang, B.; Song, D.; Li, G.; Zhang, B. An experimental study of the morphological evolution of pyrite under hydrothermal conditions and its implications. *J. of Geochem. Explor.* **2020**, *219*, 106636.

(12) Wilkin, R. T.; Barnes, H. L.; Brantley, S. L. The size distribution of framboidal pyrite in modern sediments: An indicator of redox conditions. *Geochim et Cosmochim A* **1996**, *60* (20), 3897−3912.

(13) Fathy, D.; Wagreich, M.; Sami, M. Geochemical Evidence for Photic Zone Euxinia During Greenhouse Climate in the Tethys Sea, Egypt. In *Advances in Geophysics, Tectonics and Petroleum Geosciences, CAJG 2019*; Advances in Science, Technology & Innovation Series; Springer International: Cham; 2022, DOI: 10.1007/978-3-0-30-73026-0_85.

(14) Łukawska-Matuszewska, K.; Graca, B.; Brocławik, O.; Zalewska, T. The impact of declining oxygen conditions on pyrite accumulation in shelf sediments (Baltic Sea). *Biogeochem.* **2019**, *142*, 209−230.

(15) Dubinin, A. V.; Demidova, T. P.; Dubinina, E. O.; Rimskaya-Korsakova, M. N.; Semilova, L. S.; Berezhnaya, E. D.; Klyuvitkin, A. A.; Kravchishina, M. D.; Belyaev, N. A. Sinking particles in the Black Sea waters: Vertical fluxes of elements and pyrite to the bottom, isotopic composition of pyrite sulfur, and hydrogen sulfide production. *Chem. Geol.* **2022**, *606*, 120996.

(16) Schoonen, M. A. A. Mechanisms of sedimentary pyrite formation. January 2004. *S. Paper of the Geol. Soc, of Am.* **2004**, *379*, 117−134.

(17) Nozaki, T.; Nagase, T.; Ushikubo, T.; Shimizu, K.; Ishibashi, J.-I. Microbial sulfate reduction plays an important role at the initial stage of subseafloor sulfide mineralization. *Geol.* **2021**, *49* (2), 222−227.

(18) Shawar, L.; Halevy, I.; Said-Ahmed, W.; Feinstein, S.; Boyko, V.; Kamyshny, A.; Amrani, A. Dynamics of pyrite formation and organic matter sulfurization in organic-rich carbonate sediments. *Geochim. et Cosmochim. A* **2018**, *241*, 219−239.

(19) King, F. A review of the properties of pyrite and the implications for corrosion of the copper canister. *Tech. R.* TR-13-19, Svensk Kärnbränslehantering AB, 2013.

(20) Tao, D. P.; Richardson, P. E.; Luttrell, G. H.; Yoon, R.-H. Electrochemical studies of pyrite oxidation and reduction using freshly-fractured electrodes and rotating ring-disc electrodes. *Electrochi. A* **2003**, *48* (24), 3615−3623.

(21) Weerasooriya, R.; Tobschall, H. J. Pyrite−water interactions: Effects of pH and pFe on surface charge. Colloids and surfaces. *Physicochem. and Engr. Asp.* **2005**, *264* (1), 68−74.

(22) Pacton, M.; Gorin, G. E.; Vasconcelos, C. Amorphous organic matter — Experimental data on formation and the role of microbes. *R. of Palaeobot. and Palynol* **2011**, *166* (3−4), 253−267.

(23) Roy, M.; Martinelli, L.; Ginestar, K.; Favergeon, G. Dissolution and oxidation behaviour of various austenitic steels and Ni-rich alloys in lead-bismuth eutectic at 520 C. *J. of Nucl. Mats.* **2016**, *468*, 153−163.

(24) Battaglia, F.; Morin, D.; Ollivier, P. Dissolution of cobaltiferous pyrite by Thiobacillus ferrooxidans and Thiobacillus thiooxidans: factors influencing bacterial leaching efficiency. *J. Biotechnol.* **1994**, *32* (1), 11−16.

(25) Fowler, T. A.; Holmes, P. R.; Crundwell, F. K. On the kinetics and mechanism of the dissolution of pyrite in the presence of Thiobacillus ferrooxidans. *Hydromet.* **2001**, *59* (2−3), 257−270.

(26) Wallace, A.; Wallace, G. A. Factors influencing oxidation of iron pyrite in soil. *J. of Plant Nutri.* **1992**, *15* (10), 1579−1587.

(27) Qiu, G.; Luo, Y.; Chen, C.; Lv, Q.; Tan, W.; Liu, F.; Liu, C. Influence factors for the oxidation of pyrite by oxygen and birnessite in aqueous systems. *J. of Env. Sci.* **2016**, *45*, 164−176.

(28) Ou, L.-M.; He, R.-Q.; Feng, Q.-M. Influencing factors of pyrite leaching in germ-free system. *J. Cent. South Univ. Technol.* **2007**, *14*, 28−31.

(29) Liu, Q.; Zhang, Y.; Li, H. Influence of differential stress on the galvanic interaction of pyrite-chalcopyrite. *Ions* **2013**, *19*, 77−82.

(30) Han, Y.; Ma, X.; Zhao, W.; Chang, Y.; Zhang, X.; Wang, X.; Wang, J.; Huang, Z. Sulfur-oxidizing bacteria dominate the microbial diversity shift during the pyrite and low-grade pyrolusite bioleaching process. *J. Biosci Bioeng.* **2013**, *116* (4), 465−71.

(31) Rigby, P. A.; Dobos, S. K.; Cook, F. J.; Goonetilleke, A. 2006. Role of organic matter in framboidal pyrite oxidation. *Sci. of the Ttl Envi* **2006**, *367* (2−3), 847−854.

(32) Genik, G. J. Petroleum Geology of Cretaceous-Tertiary Rift Basins in Niger, Chad, and Central African Republic. *AAPG Bull.* **1993**, *77* (8), 1405−1434.

(33) Kabir, S. A.; Keyu, L.; Moussa, H.; Jianliang, L.; Yuchen, F. Characteristics of the Upper Cretaceous Yogou transitional formation and source rock potential, Niger rift basin. *J. of Afri. Earth Sci.* **2022**, 104632.

(34) Ahmed, K. S.; Liu, K.; Paterne, M.; Kra, K.; Kuttin, A.; Malquaire, K.; Ngum, K. Anatomy of Eastern Niger Rift Basin with Specific References of Its Petroleum Systems. *Int. J. of Geosci* **2020**, *11*, 305−324.

(35) Harouna, M.; Pigott, J. D.; Philp, R. P. Burial History and Thermal Maturity Evolution of the Termit Basin, Niger. *J. of Petro. Geol.* **2017**, *40* (3), 277−297.

(36) Lai, H.; Li, M.; Liu, J.; Mao, F.; Xiao, H.; He, W.; Yang, L. Organic geochemical characteristics and depositional models of Upper Cretaceous marine source rocks in the Termit Basin, Niger. *Palaeogeo, Palaeocli, Palaeoeco* **2018**, *495*, 292−308.

(37) Rickard, D. Sedimentary pyrite framboid size-frequency distributions: A meta- analysis. *Palaeogeo, Palaeocli, Palaeoeco* **2019**, *522*, 62−75.

(38) Limpert, E.; Stahel, W. A.; Abbt, M. Log-normal Distributions across the Sciences: Keys and Clues: On the charms of statistics, and how mechanical models resembling gambling machines offer a link to a handy way to characterize log-normal distributions, which can provide deeper insight into variability and probability—normal or log-normal: That is the question. *BioSci.* **2001**, *51* (5), 341−352.

(39) Sawlowicz, Z. Pyrite framboids and their development: a new conceptual mechanism. *Geol Rundsch* **1993**, *82*, 148−156.

(40) Merinero, R.; Cárdenes, V. Theoretical growth of framboidal and sunflower pyrite using the R-package frambgrowth. *Miner. Petrol.* **2018**, *112*, 577−589.

(41) Cavalazzi, B.; Barbieri, R.; Cady, S. L.; George, A. D.; Gennaro, S.; Westall, F.; Lui, A.; Canteri, R.; Rossi, A. P.; Ori, G. G.; Taj-Eddine, K. Iron-framboids in the hydrocarbon-related Middle Devonian Hollard Mound of the Anti-Atlas mountain range in Morocco: Evidence of potential microbial biosignatures. *Sed. Geol.* **2012**, *263−264*, 183−193.

(42) Duverger, A.; Berg, J. S.; Busigny, V.; Guyot, F.; Bernard, S.; Miot, J. Mechanisms of Pyrite Formation Promoted by Sulfate-Reducing Bacteria in Pure Culture. *Front. Earth Sci.* **2020**, *8*, 588310.

(43) Ohfuji, H. Structure of framboidal pyrite: An electron backscatter diffraction study. *Am. Mineral.* **2005**, *90* (11−12), 1693−1704.

(44) Liu, Z.; Chen, D.; Zhang, J.; Lü, X.; Wang, Z.; Liao, W.; Shi, X.; Tang, J.; Xie, G. Pyrite Morphology as an Indicator of Paleoredox Conditions and Shale Gas Content of the Longmaxi and Wufeng Shales in the Middle Yangtze Area, South China. *Min.* **2019**, *9* (7), 428.

(45) Wendorff-Belon, M.; Rospondek, M.; Marynowski, L. Early Oligocene environment of the Central Paratethys revealed by biomarkers and pyrite framboids from the Tarcău and Vrancea Nappes (Eastern Outer Carpathians, Romania). *Mar. and Petr. Geol* **2021**, *128*, 105037.

(46) Schallreuter, R. Framboidal Pyrite in Deep-Sea Sediments. Geologisch-Palàontologisches Institut und Museum, University of Hamburg: 1982. Accessed August 10, 2021.

(47) Wignall, P. B. Sedimentary Environment I Anoxic Environment. *Encycl. of Geol* **2005**, 459−501.

(48) Jiang, K.; Zhou, W.; Deng, N.; Song, W. Statistical analysis and significance of pyrite in the Wufeng-Lower Longmaxi Shale Formation in South China. *Arab J. Geosci.* **2020**, *13* (2020), 1181.

(49) Courtin-Nomade, A.; Bril, H.; Bény, J.-M.; Kunz, M.; Tamura, N. Sulfide oxidation observed using micro-Raman spectroscopy and micro-X-ray diffraction: The importance of water/rock ratios and pH conditions. *Am. Mineral.* **2010**, *95*, 582−591.

(50) Gu, X.; Heaney, P. J.; Reis, F. D. A. A.; Brantley, S. L. Deep abiotic weathering of pyrite. *Sci.* **2020**, *370* (6515), eabb8092.

(51) Raiswell, R.; Berner, R. A. Pyrite formation in euxinic and semi-euxinic sediments. *Am. J. Sci.* **1985**, *285* (8), 710−724.

(52) Schieber, J. Iron Sulfide Formation. *Encyclopedia of Geobiology*; Reitner, J., Thiel, V., Eds.; Springer: 2011; pp 486−502.

(53) Weisener, C. G.; Weber, P. A. Preferential oxidation of pyrite as a function of morphology and relict texture. *New Zealand J. of Geol. and Geophy.* **2010**, *53* (2−3), 167−176.

(54) Kim, J. G.; Woo, I.; Lee, G. H.; Park, H. J.; Um, J. G. Evaluation of the impact of pyrite oxidation on rock characteristics and environment by laboratory tests. *Env. Earth. Sci.* **2013**, *69*, 1821−1829.